Pulmonary lobar segmentation from computed tomography scans based on a statistical finite element analysis of lobe shape

****

****

****

****

Abstract

Automatic identification of pulmonary lobes from imaging is important in lung disease assessment and treatment planning. However, the pulmonary lobar fissure can be difficult to detect automatically, as it is thin, usually of fuzzy appearance and incomplete, and can be obscured by or confused with features of disease. In this study, we aim to overcome difficulties in identifying pulmonary fissures by using a statistical finite element shape model of the lungs and lobar fissures to guide lobar segmentation. By deforming a statistical shape model onto an individual's lung shape, we predict the likely region of fissure locations, to initialize the search region for fissures. Then, an eigenvalue of Hessian matrix analysis and a connected component eigenvector based analysis are used to determine a set of fissure-like candidate points. A smooth multi-level B-spline curve is fitted to the most fissure-like points (those with high fissure probability) and the fitted fissure plane is extrapolated to the lung boundaries. The method was tested on 20 inspiratory and expiratory CT scans in healthy young subjects and older subjects with idiopathic pulmonary fibrosis. A quantitative comparison to manually-segmented fissures gave mean differences of left oblique, right horizontal and right oblique fissures of 2.06 mm, 4.06 mm and 2.85 mm (respectively) for healthy cases and 3.41 mm, 5.79 mm and 5.01 mm (respectively) for pathological cases. The method was able to estimate the fissure location in 100% of cases, whereas two other segmentation softwares which use watershed-based method tested for comparison were unable to segment 7/20 and 9/20 subjects respectively (1/10 and 2/10 normal and 6/10 and 7/10 pathological).

1 Introduction

Human lungs are divided into five lobes which form distinct anatomical regions separated by fissures. Identification of these lobes in imaging is important for assessment of lung disease severity and treatment planning. The lobes act somewhat independently of each other with respect to respiratory function, thus many pulmonary diseases act at a lobar level [1]. For example, emphysema, postprimary tuberculosis and silicosis usually affect the upper lobes, while idiopathic pulmonary fibrosis commonly presents in the lower lobes. For clinical applications, identification of the pulmonary fissures can be an important step in the image-based study of lung function and disease: knowing the lobar distribution of pulmonary disease is beneficial for doctors to recognize pathogenesis and guide therapy (including surgical planning) [2]. Segmentation of lobes can also facilitate intra-patient image registration for localizing and tracking disease progression, since lobes are

important landmarks. However, the lobes are difficult to segment automatically as they can appear as faint or fuzzy lines in imaging, fissures can be incomplete (even in healthy patients), and there is anatomical variation in lobe shape and size between individuals. This anatomical variation is usually associated with age, sex, height and body mass index (BMI) [3] [4].

In a broad sense, existing algorithms that aim to automatically segment pulmonary lobes consist of two steps: lung segmentation and fissure detection. Lung segmentation methods are well-established and results are typically reliable [5] [6]. In contrast, automated fissure detection is challenging. Some proposed fissure detection methods make use of either local or global knowledge of lung anatomy, such as airway and vessel trees, to identify fissures [1] [7] [8]. For example, there are typically no large vessels in the vicinity of lobar fissures, so fissures should be located in the gaps between airway and vessel trees. These methods can be time consuming to execute as airways and blood vessels must be identified as an intermediate step. If the airways or vessels cannot be segmented – for example, due to tissue abnormalities or failure division of airway main braches, then these methods cannot complete the fissure segmentation. A second class of fissure detection algorithm makes use of gray-level information and shape information to detect the fissures [2] [3] [9]. Generally, lobar fissures can be regarded as bright planes crossing the pulmonary volume because of the higher density value of fissures compared to the surrounding tissues. Based on this information, several published methods use a local filtering algorithm to detect the voxels which lie on these planes, so that these detected voxel points can construct a continuous fissure surface. These algorithms often face problems when lobe fissures are blurry or incomplete. A further challenge for all segmentation methods is identifying the fissures in thin-slice CT that has large spacing between slices.

In this paper, we present a statistical finite element shape model-guided method to segment pulmonary lobes from CT images. This new procedure does not depend on prior segmentation of anatomical structures (airway lobar classification) and has promising potential as a clinically useful semi-automatic lobe segmentation procedure.

2 Methods

A three-step approach is followed for the lobe segmentation (Fig 1): in the first step, a threshold-based lung segmentation method defines the lung boundary; in the second step, a statistical shape model (SSM) is deformed to provide a ‘search region’ for fissure locations; in the third step, fissures are located using a Hessian matrix protocol combined with connected component filters and a surface fitting algorithm.

2.1 Lung segmentation

A commonly used thresholding method is used to segment the lungs [5]. The method uses a thresholding operation (-775 Hounsfield Units) and connected component identification to find an initial approximation to the lung regions and trachea location. Using the most apical point of the trachea as a start point, a region growing technique is applied to detect the airway trees. Then, left and right lungs are separated as the two largest connected components remaining after removing the trachea and the left and right main bronchi.

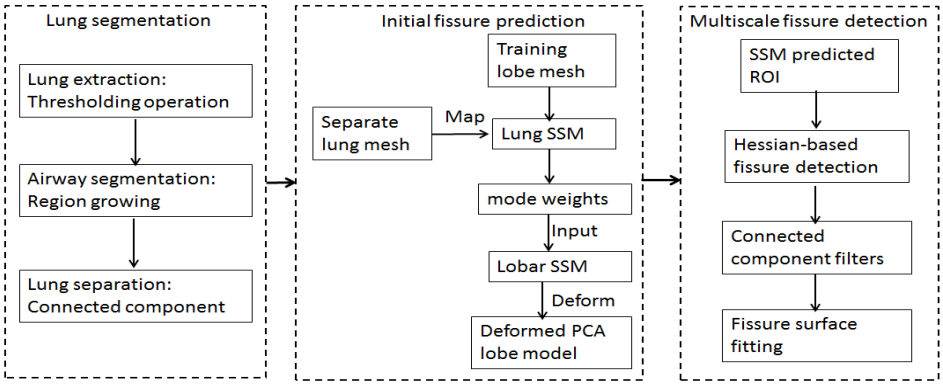

Fig. 1. Flow diagram of the lobar segmentation process.

2.2 Statistical finite element models of lung and fissure shape

To guide fissure detection, a statistical shape model (SSM) based on an active shape model (ASM) [10] of the lung was derived from a training set of segmented lung and fissure surface locations. The training set consisted of data from 30 healthy non-smokers (15 males and 15 females) that was retrospectively selected from the Human Lung Atlas (HLA) database (image acquisition for this previous study was approved by the local ethics and radiation safety committees, and subjects gave informed consent). Lung surface segmentation was conducted as described in section 2.1; fissure surface segmentation was performed manually using the open-source visualization software CMGUI (https://www.cmiss.org/cmgui) by an expert user, to provide a gold-standard definition of the fissure location for each subject in the training set.

A finite element surface mesh was used to describe the shape of the lung and its fissures in terms of the ASM (and, in section 2.3, to define initial fissure location in the segmentation algorithm). A high order (bi-cubic Hermite) finite element mesh template with the same mesh connectivity for each subject was geometry fitted to the lung and fissure surface data for each subject. The template mesh for the left lung mesh has 35 nodes and 44 elements, while the right lung mesh has 50 nodes and 62 elements. Each node has 12 degrees of freedom (DoF) which store the global coordinates and first and second nodal derivatives. Each node is either an anatomical landmark (the left/right lung apex, the base vertex, the shape corner and the center point of the middle line of fissure) or a pseudo-landmark (e.g. a specific proportion of the arc-length between two anatomical landmarks). A least squares fit of the mesh to the lung and fissure surface data was conducted using CMISS (https://www.cmiss.org), which is a finite element modeling environment. The average root mean square (RMS) error of this fitting method was 0.52 mm for the 30 training subjects (Fig 2(a)).

To construct the SSM, the location and derivatives at each node (landmark or pseudo-landmark) in the finite element mesh was used in a principal component analysis (PCA) conducted on the training set. To remove orientation and scaling differences between shapes, a general procrustes alignment (GPA) method was used to minimize the distance between subject meshes through calculating an optimal rotation matrix and translation (Fig 2(b)) [11]. The volumes of all subjects were normalized to 1 L during processing. The procrustes aligned mesh was represented by

$$\mathrm{B} = [\overline{x_1}\ \overline{y_1}\ \overline{z_1}\ \overline{x_2}\ \overline{y_2}\ \overline{z_2} \cdots \overline{x_p}\ \overline{y_p}\ \overline{z_p}],$$

where p is the total number of nodes of all the subjects (2550 nodes for our study, for 30 subjects in total), and the over-line represents GPA to the mean. The matrix B was decomposed into modes of shape variation by a PCA. PCA is a statistical procedure that uses an orthogonal transformation to find the principle modes of variation in a sample, through analyzing the eigenvectors and eigenvalues of the covariance matrix of the data matrix B. In this study each mode represents one type of lung and fissure surface shape variation. The first seven principal components accounted for over 90% of the total variation in the training set. The PCA provides a definition of a statistically averaged lung and fissure surface shape, which is the statistical shape model (SSM) that is referred to in the following sections. A second SSM was derived for the training set that did not include the fissure surfaces and so only described the shape of the lung surface.

2.3 Initial prediction of lobar location in an individual

The two SSMs were used to predict the fissure locations for subjects that were not part of the training set, using only the definition of the lung surface for the subject as input. A finite element mesh of the lung surface (without fissure information) was generated for a new subject. This lung surface mesh was projected on to the lung surface SSM (with no fissure surfaces). The principal component weight values were calculated from the projection and these weights were used to deform the SSM that contained both lung and fissure surfaces to the subject, to give an initial estimation of fissure locations (Fig 2(c) (d)). This initial prediction of lobar fissures provides a reduced search area for subsequent image analysis and ensures an estimation of complete lobar structures even if a fissure is incomplete or is difficult to detect in a small region of the image.

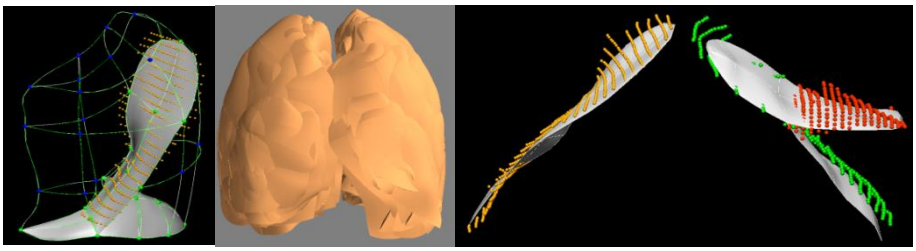

(a) (b) (c) (d)

Fig. 2. SSM initial fissure prediction results. (a) Lung surface fitting and manually-digitized fissure data. (b) Procrustes aligned meshes of 30 subjects. (c) (d) Fissure prediction (white) compared to ground truth fissure points.

2.4 Multiscale Hessian-based fissure detection

The location of the SSM predicted fissure planes (Fig 2 (c)(d) were used to guide a Hessian based fissure detection in an individual. Gaussian filters with kernel sizes from 0.5-2.5 mm in 0.5 mm increments were applied to the image set. The responses at each kernel were combined to get a maximum response for each voxel of the image. This multiscale operation guarantees fissures of variable size can be captured by Hessian operations. At each image voxel, the Hessian matrix was constructed as a symmetric matrix. For a fissure structure, which presents as a light plane on a dark background, two large positive second derivatives across the plane and a small second derivative (of either sign) along the plane are expected. This is reflected in the Hessian matrix as two small eigenvalues corresponding to the eigenvectors along the fissure planes and one large eigenvalue perpendicular to the plane. Thus with the relationship of eigenvalues $\lambda_1, \lambda_2, \lambda_3$ defined as $|\lambda_1| \leq |\lambda_2| \leq |\lambda_3|$, λ_3 is expected to be much larger than λ_1 and λ_2 at the fissure. From these

characteristics, the fissure probability of each voxel is

$$S = \tau S_{plane} S_{wall}.$$

The parameter τ supresses points whose largest eigenvalue λ_3 is positive, since fissures are locally bright , and is defined as

$$\tau = \begin{cases} 1, & \lambda_3 < 0, \\ 0, & \lambda_3 \geq 0. \end{cases}$$

S_{plane} detects plane or curve-like structures by searching for locations where $|\lambda_3|$ and $|\lambda_2|$ are significantly different:

$$S_{plane} = \exp(-\frac{{R_{plane}}^2}{2p^2}),\ R_{plane} = \frac{|\lambda_2|}{|\lambda_3|}.$$

S_{wall} suppresses signal of noise and 'blob-like' structures:

$$S_{wall} = \exp(-\frac{{R_{noise}}^2}{2w^2}),\ R_{noise} = \sqrt{\lambda_1^2 + \lambda_2^2 + \lambda_3^2}.$$

p and w are both set to 0.5 as thresholding in this study. S then gives a high response to local sheet-like structures (fissures) and suppresses other pulmonary structures. An example of this filter applied in an individual is shown in Fig 3(a). Blood vessels, which appear as similar structures locally to fissures, are removed from the fissure enhanced result using previous described methods, which removes tube-like structures with $|\lambda_1| \approx 0$, $|\lambda_1| \ll |\lambda_2|$, $|\lambda_2| \approx |\lambda_3|$ (Fig 3(b)) [12].
The fissure location predicted by this method allows definition of a search region for the fissure (Fig 3(c)). Candidate points were selected within a fixed distance of the initial fissure approximation: the search distance was set to 20 voxels for left and right oblique fissures and 15 voxels for right horizontal fissure initially. A 2D 4-neighborhood connected component filter and a 3D 6-neighborhood vector-based connected component filter were employed successively to eliminate noise arising from small plane-like structures in this search region (Fig 3(d)). The vector-based connected component filter uses the inner product of the normalized largest eigenvector of the Hessian matrix in adjacent voxels. These largest eigenvectors are perpendicular to the fissure plane, and their inner product provides a criterion for component connection. As the curvature of a fissure is locally low, adjacent fissure voxels should have similar largest eigenvectors and thus large inner product values.
The detected points were then divided into a set of small subsections corresponding to different x, y intervals. For each subsection, the point of the highest fissure probability (the highest S value) was selected as the final candidate fissure point (Fig 3(e)). Then a continuous smooth fissure surface was generated using a B-spline method with a thin-plane spline and extrapolated to the lung boundaries, see Fig 3(f).

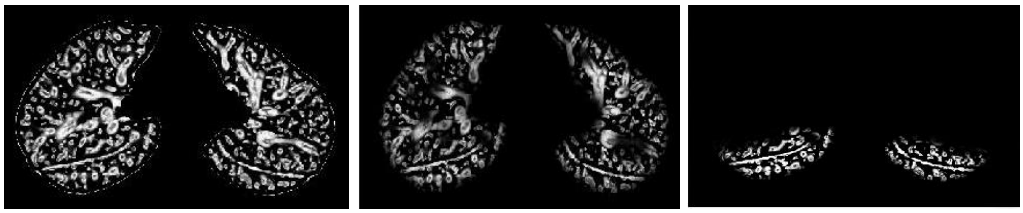

(a) (b) (c)

(d) (e) (f)

Fig. 3. Hessian-based multiscale fissure detection results. (a) Hessian-based fissure enhancement. (b) Remove vessel voxels. (c) ROI of fissure locations based on SSM projection. (d) 2D and 3D eigenvector based connected component filter. (e) Fissure candidate points. (f) B-spline curve fissure surface fitting.

3 Experiment

3.1 Data

The semi-automatic method was tested on two datasets: 1) CT images from five young normal volunteers taken at different lung volumes (end inspiration and end expiration) and with a range of slice thickness (0.5-0.7 mm); 2) CT images from older patients (slice thickness 1.25-3.00 mm) acquired during routine diagnostic inspection for idiopathic pulmonary fibrosis (IPF). Access to clinical data was approved by the Southern Health and Disability Ethics Committee.

3.2 Results

The ability of the method to provide an initial estimate of the fissure locations was compared with an interactive watershed transform method [6]. We tested two watered-based segmentation softwares here: 1. Pulmonary Toolkit, https://github.com/tomdoel/pulmonarytoolkit; 2. Pulmonary Analysis Software Suite [14]. The two segmentation softwares tested for comparison were unable to segment 7/20 and 9/20 subjects respectively (1/10 and 2/10 normal and 6/10 and 7/10 IPF subjects). In contrast, the model-based method gave an initial estimate for all subjects at all volumes.

To quantitatively assess the accuracy of the lobar segmentation method in the normal and IPF subjects, the semi-automatic segmentation was compared with 'gold-standard' manual segmentations. Segmentation accuracy was quantitatively evaluated by computing the mean difference and percentage of fissure points <3 mm between the gold-standard and semi-automatic method (Fig 4). The 3 mm criterion approximates the thickness of CT images routinely used clinically [13].

For normal subjects, the average mean differences (and accuracies) were 2.06 mm (78%), 4.06 mm (62%), and 2.85 mm (72%), for left oblique, right horizontal and right oblique fissures, respectively. For IPF subjects, the average mean differences (and accuracies) were 3.41 mm (66%), 5.79 mm (56%), and 5.01 mm (60%), for left oblique, right horizontal and right oblique fissures, respectively.

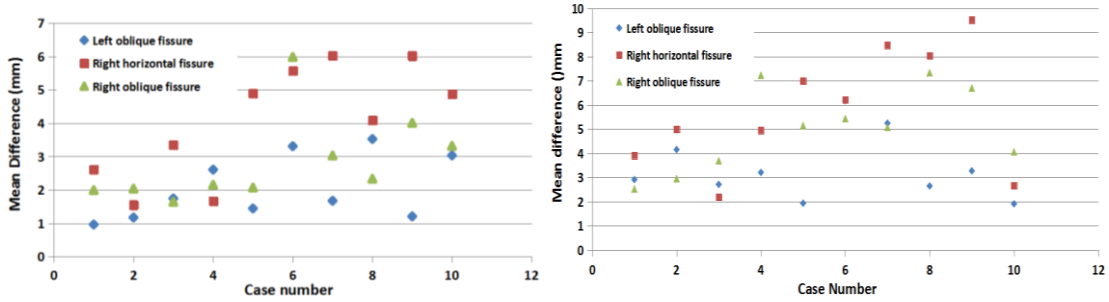

(a) (b)

Fig. 4. Quantitative evaluation results of the segmentation accuracy. (a) Mean difference for normal young subjects. (b) Mean difference for IPF subjects.

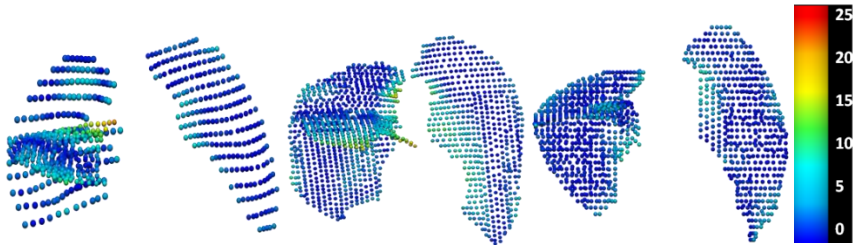

(a) (b) (c)

Fig. 5. The spatial distribution of error between the gold-standard and semi-automatic methods for three representative subjects, highlighting localized regions of low accuracy.

Fig 5 shows the spatial distribution of error for three representative subjects. Error was highest in regions close to the hilum (where the anatomical structures are complex, and/or the fissure is often incomplete), and where the right fissures meet.

4 Conclusions and Discussion

In this paper, we presented a pulmonary lobar segmentation method. Results show that the method can perform well to detect the location of the fissures over most of the fissure surfaces on CT images from normal subjects, and provides a relatively accurate result for most of the IPF (abnormal) subjects. Due to lower imaging resolution and tissue abnormalities, the accuracy of the method was lower for the IPF subjects.

The method performed better on the left oblique fissure than the other two fissures, because the left lung has a simpler anatomic structure with only one fissure. In contrast, misdetection happens more often in the area of right lung where the two fissures come into contact. This is illustrated in Fig 5, which shows the error distribution over the three fissures for three subjects. It can also be seen that the method results in higher error in the lung boundary area, since the fissures here are commonly incomplete, thus few fissure candidate points can be detected accurately.

Compared to the current published anatomical structure-based methods, the model-based method can predict an initial fissure location without requiring an accurate preliminary analysis of other anatomical features. For example, traditional anatomical knowledge-based methods such as the watershed-based lobar segmentation need to label the airway trees to the five main lobar bronchi to get an initial fissure approximation. However, due to the complex radiological appearance of

pathological lungs, it is usually difficult to get a reliable airway and vessel tree segmentation. This was the case in our comparison of the model-based estimation of fissure location with a watershed-based method; the latter failed for nearly half of the subjects.

References

1. Ukil S., Reinhardt J.M.: Anatomy-guided lung lobe segmentation in x-ray CT images. IEEE Transaction Medical Imaging 28(2), 202-214 (2009)
2. van Rikxoort E.M., Prokop M., de Hoop B., Vierggever M.A., Pluim J.P.W., van Ginneken B.: Automatic segmentation of pulmonary lobes robust against incomplete fissures. IEEE Transaction Medical Imaging 29(6), 1286-1296 (2010)
3.Ross J.C, San J.E.R., KindImann G., Diaz A., Westin C.F., Silverman E.K.: Automatic lung lobe segmentation using particles, thin plate splines, and maximum a posteriori estimation. Medical Image Computing and Computer-Assisted Intervention. 13(3) 163-171 (2010)
4. Gülsün M., Ariyürek O., Cömert R., Karabulut N.: Variability of the pulmonary oblique fissures presented by high-resolution computed tomography. Surgical and Radiologic Anatomy. 28(3) 293–299 (2006)
5. Ukil S., Reinhardt J.M.: Smoothing lung segmentation surfaces in three-dimensional x-ray CT images using anatomic guidance. Academic Radiology. 12(12) 1502-1511 (2005)
6. Sun S., Bauer C., Beichel R.: Automated 3-D segmentation of lungs with lung cancer in CT data using a novel robust active shape model approach. IEEE Transaction Medical Imaging. 31(2) 449-60 (2012)
7. Doel T., Matin T.N., Gleeson F.V., Gavaghan D.J., Grau V.: Pulmonary lobe segmentation from CT images using fissureness, airways, vessels and multilevel B-splines. 9th IEEE International Symposium on Biomedical Imaging 1491-1494 (2012)
8. Lassen B., van Rikxoort E.M., Schmidt M., Kerkstra S., van Ginneken B., Kuhnigk J.: Automatic segmentation of the pulmonary lobes from chest CT scans based on fissures, vessels, and bronchi. IEEE Transaction Medical Imaging 32(2) 210-22 (2013)
9. Kitasaka T., Nakada Y., Mori K., Suenaga Y., Mori M., Takabatake H., Natori H.: Recognition of lung lobes and its application to the bronchial structure analysis. 18th International Conference on Pattern Recognition (ICPR'06) 288-291 (2006)
10. Cootes T.F., Taylor C.J., Cooper H.D., Graham J.: Active shape models-their training and application. Computer Vision and Image Understanding 61 38-59 (1995)
11. Rohlf F.J.: Shape statistics: Procrustes supermpositions and tangent spaces. Journal of Classification 16 197-223 (1999)
12. Frangi A.F., Niessen W.J., Vincken K.L., Viergever M.A.: Multiscale vessel enhancement filtering. Medical Image Computing and Computer-Assisted Intervention 130-137 (1998)
13. Qiao W.: Segmentation of lung lobes in high-resolution isotropic CT images. IEEE Transactions on Biomedical Engineering 56(5) (2009)
14. Guo J.F., Fuld M.K., Alford S.K., Reinhardt J.M., Hoffman E.A,: Pulmonary analysis software suite 9.0: Integrating quantitative measures of function with structural analyses. First international workshop on pulmonary image processing 283-292 (2009)